

Long-term noise interferometry analysis in the northeast Pacific Ocean

John Ragland, Shima Abadi and Karim Sabra

Citation: [The Journal of the Acoustical Society of America](#) **151**, 194 (2022); doi: 10.1121/10.0009232

View online: <https://doi.org/10.1121/10.0009232>

View Table of Contents: <https://asa.scitation.org/toc/jas/151/1>

Published by the [Acoustical Society of America](#)

**Get a first look at
the new release of
COMSOL Multiphysics®**
at a free, online event

[JOIN US »](#)

JANUARY 27, 2022



COMSOL Day
Version 6.0

Long-term noise interferometry analysis in the northeast Pacific Ocean

John Ragland,^{1,a)} Shima Abadi,^{1,b)} and Karim Sabra^{2,c)}

¹*Electrical and Computer Engineering, University of Washington, Seattle, Washington 98195, USA*

²*Mechanical Engineering, Georgia Institute of Technology, Atlanta, Georgia 30332, USA*

ABSTRACT:

Long-term noise interferometry analysis is conducted over six years of data using two hydrophones on the Ocean Observatories Initiative Cabled Array. The two hydrophones are separated by 3.2 km and are bottom-mounted at 1500 m. We demonstrate the ability of ambient noise interferometry to reliably detect multi-path arrivals in the deep ocean from bottom-mounted hydrophones. An analysis of the multi-path arrival peak emergence is presented, as well as long-term trends of the signal-to-noise ratio of the arrival peaks. Last, we show that long-term ambient noise interferometry provides the opportunity for monitoring directional, coherent ambient sound such as the fin whale chorus.

© 2022 Author(s). All article content, except where otherwise noted, is licensed under a Creative Commons Attribution (CC BY) license (<http://creativecommons.org/licenses/by/4.0/>). <https://doi.org/10.1121/10.0009232>

(Received 19 August 2021; revised 18 November 2021; accepted 9 December 2021; published online 10 January 2022)

[Editor: John A. Colosi]

Pages: 194–204

I. INTRODUCTION

Ambient noise interferometry is a well-developed method for passively estimating the time domain Green's function (TDGF) using ambient sound. It was first demonstrated by [Weaver and Lobkis \(2001\)](#) and has been further developed by many other works in the field ([Godin, 2009, 2010, 2018](#); [Roux and Kuperman, 2004](#); [Roux et al., 2005](#); [Sabra et al., 2005b](#); [Weaver and Lobkis, 2004, 2005](#)). Ambient noise interferometry has found many applications in seismology and oceanography. Some applications to seismology include the measurement of dispersion curves, characterizing basin resonance, estimating the source location of earthquakes, and estimating the surface wave velocity structure ([Bensen et al., 2007](#); [Boué et al., 2016](#); [Denolle et al., 2013](#); [Sabra et al., 2005a](#)). Some applications to acoustic oceanography include measuring the ocean temperature, measuring ocean current velocities, and exploring time reversal techniques ([Brown et al., 2016](#); [Evers et al., 2017](#); [Godin et al., 2017](#); [Goncharov et al., 2015](#); [Sambell et al., 2019](#); [Woolfe et al., 2015](#)).

Previous work in ambient noise interferometry has shown the possibility of estimating the TDGF in the shallow ocean ([Brown et al., 2014](#); [Roux and Kuperman, 2004](#)). Noise interferometry has also been demonstrated in the deep ocean by utilizing the Sound Fixing and Ranging (SOFAR) channel to measure the direct path ([Woolfe and Sabra, 2015](#)). Due to long-term measurement platforms like the Ocean Observatories Initiative (OOI), ocean ambient noise data has become more available in recent years. As a result,

the opportunity to use these data along with ambient noise interferometry for global oceanographic monitoring is extremely promising. The configuration of hydrophones for these long-term measurement platforms usually includes sparse arrays of bottom mounted hydrophones in the deep ocean, which have not been extensively investigated for applications in ambient noise interferometry. Specifically, multi-path arrivals in the deep ocean have not previously been distinguished using ambient noise interferometry. In this paper, publicly available ambient noise data from bottom-mounted hydrophones in the OOI network will be used to estimate the TDGF. The feasibility of using ambient noise interferometry for a short range (3.2 km) and deep ocean (1500 m) to resolve multi-path arrivals will be demonstrated. Additionally, the quality of ambient noise interferometry for this specific hydrophone configuration and ambient noise source distribution will be quantified for six years of ambient noise data.

The TDGF estimate emerges from a noise cross correlation function (NCCF), which consists of time averaged cross-correlations between the two receivers. The emergence of the TDGF in an NCCF can be intuitively explained by considering sound that travels through both hydrophones. Sound that is received by the first hydrophone, then propagates through the ocean between the two hydrophones, and is last received by the second hydrophone would produce a peak in the cross correlation of the two signals. The location of this peak in the cross correlation is the time it took the acoustic signal to travel through the ocean from the first hydrophone to the second hydrophone. Noise sources that contribute to these peaks are located in the endfire direction of the hydrophone array. If cross-correlations are averaged together, contributions for sources not located in the end-fire direction of the two hydrophones are averaged out and the

^{a)}Electronic mail: jhrag@uw.edu, ORCID: 0000-0001-9246-2269.

^{b)}Also at: Division of Engineering and Mathematics, University of Washington, Bothell, WA 98011, USA.

^{c)}ORCID: 0000-0003-4191-3044.

TDGF emerges in the NCCF (Sabra *et al.*, 2005b; Weaver and Lobkis, 2004).

One of the primary contributors to ambient sound in the frequency band of 1–90 Hz is from shipping noise (Urick, 1975; Wenz, 1962), which originates near the surface of the ocean. It has been shown that with a spatially uniform surface distribution of sound sources, the derivative of the NCCF converges to an amplitude weighted TDGF (Roux and Kuperman, 2004; Sabra *et al.*, 2005b). The TDGF can be approximated by Eq. (1), where τ is delay time, $C(\tau)$ is the NCCF, $D(\tau)$ is an approximation of the delta function and is dependent on $C(\tau)$ the spectrum and spatial distribution of the ambient noise sources, and $G_{AB}(\tau)$ is the TDGF from node A to node B (Brown *et al.*, 2014; Roux *et al.*, 2005),

$$\frac{\partial C_{AB}(\tau)}{\partial t} \sim D(\tau) \star [G_{AB}(\tau) - G_{BA}(-\tau)]. \quad (1)$$

The emergence of the TDGF in the NCCF can be explained by acoustic signals from the same source physically passing through one hydrophone and then propagating through the ocean to the second hydrophone. Skarsoulis and Cornuelle (2019) showed with simulation that the acoustic propagation environment plays a large role in whether a TDGF is discernible in an NCCF. Since the primary contributors to ambient sound in the frequency band of the experiment originate from the ocean surface, the sound contributing to the direct path propagation is likely from distant, surface sources. This has been demonstrated experimentally for hydrophones in the SOFAR channel (Woolfe and Sabra, 2015). Conversely, sound contributing to the emergence of multi-path acoustic arrivals originate from local surface sources with steep angles of propagation. This was demonstrated in the shallow ocean by using the coherent sound from a tropical storm (Brooks and Gerstoft, 2009). This means that the sound sources contributing to the direct and multi-path arrivals are located in different places relative to the hydrophones. Therefore, the two main contributing factors to whether an experiment is suitable for direct and multi-path acoustic propagation measurement using ambient noise interferometry are if the acoustic propagation environment and the spatial distribution of coherent sound sources are favorable.

Brooks and Gerstoft (2009) and Brown *et al.* (2014) demonstrate the feasibility of measuring multi-path propagation paths between hydrophones in a shallow ocean environment. Evers *et al.* (2017), Sambell *et al.* (2019), and Woolfe and Sabra (2015) demonstrate the feasibility of measuring the direct acoustic propagation in the deep ocean by utilizing the SOFAR channel. In this paper, ambient noise interferometry will be explored for measuring direct, surface and surface-bottom reflected propagation paths for hydrophones located in the deep ocean (1500 m) and separated by ~ 3.2 km. A study of the emergence of the TDGF will be presented and compared to previous theoretical and experimental results. The calculated NCCFs will then be stacked

over six years and the effects on the NCCF stack from different occurrences in the ocean acoustic environment will be explored.

In Sec. II, the hydrophone environment will be described, the data processing methods used for ambient noise interferometry analysis will be discussed, and acoustic simulation of the environment will be presented. Section III analyzes the emergence of the TDGF in the NCCF, the long-term signal-to-noise ratio of different arrival peaks, and the long-term NCCF stack. Section IV discusses several known occurrences in the ocean that are visible in the long-term NCCF stack as well as identifying unknown patterns that are present in the long-term NCCF stack. Last, Sec. V summarizes the findings that are presented in this paper as well as discusses the applications and future directions of this work.

II. EXPERIMENTAL SETUP AND DATA PROCESSING

In Secs. IIA and IIB, the hydrophone geometries, acoustic environment, data processing methods, and acoustic simulation will be presented.

A. Acoustic environment

Acoustic data from two hydrophones located on the Axial Seamount volcano were used for long-term noise interferometry analysis. These hydrophones are part of the OOI Cabled Array. The first hydrophone, referred to below as the *Central Caldera* hydrophone,¹ is located at 45.95468 N, 130.00893 W and is on the seafloor at a depth of 1528 m. The second hydrophone, referred to below as the *Eastern Caldera* hydrophone,² is located at 45.93967 N, 129.97378 W and is on the seafloor at a depth of 1519 m. These two hydrophones are separated by 3.2 km. Conductivity, temperature and depth (CTD) data for acoustic simulation was used from the *Axial Base* ocean profiler, which is 24 km from the caldera hydrophones. A map of the hydrophones and CTD sensors, as well as a six-year average sound speed profile is shown in Fig. 1. Sound sources that contribute to the emergence of TDGF peaks are located in the endfire directions of the hydrophone array (Larose *et al.*, 2006; Sabra *et al.*, 2005b). Figure 2 shows the endfire directions $\pm 10^\circ$ for the *Central Caldera* and *Eastern Caldera* hydrophones. Acoustic data between January 2015 and December 2020 was used. Both hydrophones have a sampling rate of 200 Hz.

The ambient sound at both hydrophones was studied to better understand what sound sources contribute to the emergence of the TDGF estimate. Figure 3 shows the six-year average power spectral density (PSD) for the *Central Caldera* and *Eastern Caldera* hydrophones and common occurrences in spectrograms of ambient sound. The spectrograms and six year PSDs are created from six years of data where 15 min, 512 point PSDs are estimated with the Welch median technique (Schwock and Abadi, 2021). The spectrum of the ambient noise is fairly flat between 30 and 90 Hz. The peak at 20 Hz is due to seasonal vocalizations from fin whales (Watkins *et al.*, 1987). The peak below 1 Hz is due to microseisms (Webb, 1992). Individual ship passes

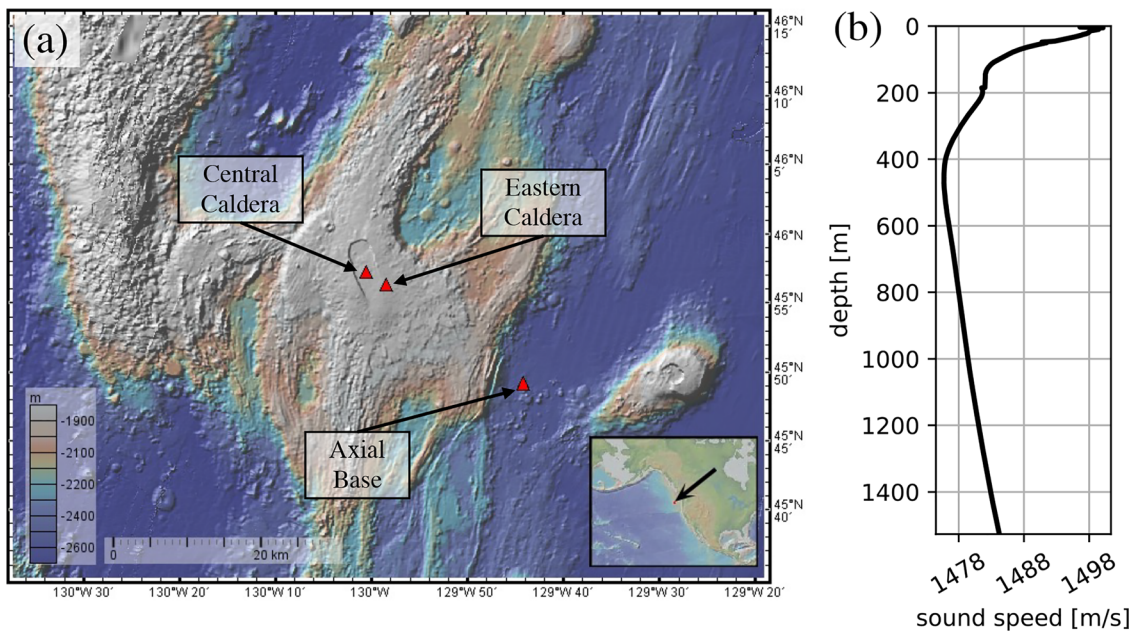


FIG. 1. (Color online) (a) Map of OOI Cabled Array sensor packages used in this paper. Hydrophones used for noise interferometry are located at Eastern Caldera and Central Caldera sensor packages. CTD casts were used from the Axial Base sensor package. (b) Six year average sound speed profile measured at the *Axial Base* location.

can be seen throughout the six years of data with energy between approximately 5 and 90 Hz. Spectral levels above 90 Hz are attenuated by a physical filter on the two hydrophones. Seasonal fin whale vocalizations centered at 20 Hz are also present from approximately November to February.

B. Acoustic data processing

The hydrophone data used for this paper is archived at the Incorporated Research Institutions for Seismology Data Management System (IRIS)³ and the Ocean Observatories Initiative (OOI) Data Portal. Acoustic data were downloaded from OOI and converted to a python ready format

using the python package OOIPy ([Schwock et al., 2021](#)). The audio from each hydrophone was preprocessed to increase the coherent noise as much as possible and to decrease the effects of spurious events in the ocean. Different types of pre-processing are explored in depth in [Groos et al. \(2012\)](#). The pre-processing methods used in this paper are similar to the techniques used in [Woolfe and Sabra \(2015\)](#) and are described in detail next.

The uncalibrated audio data for each hydrophone was first broken up into 30 s segments (consisting of 6000 points) and filtered between 1 and 90 Hz using a 4th order, zero-phase Butterworth filter. A window length of 30 s was chosen to include relevant arrival times. The signals were then clipped to three times the standard-deviation of the signal for a given hour of audio recording to help mitigate the negative effects of spurious events on the emergence of the TDGF estimates. Lastly, the individual signals were frequency whitened. To frequency whiten the signals, the time domain signal was windowed with a Hann window and then the 6000 point discrete Fourier transform was computed. The magnitude of the signal spectra is replaced with the magnitude response of an 8th order Butterworth filter (the same magnitude response as the filter used previously), and the inverse discrete Fourier transform of the signal is then computed. This preserves the phase information of the signal but makes the magnitude response flat for all relevant frequency. The pre-processing methods are outlined in Fig. 4, along with 30 s of time data before and after pre-processing. The pre-processed signals from the Central Caldera and Eastern Caldera hydrophone are then cross-correlated, resulting in a 60 s, 11 999 point signal. These 60 s long correlations are then averaged together and normalized in amplitude to create an NCCF. Averaging times will be discussed in Sec. III A.



FIG. 2. (Color online) Endfire bearings $\pm 10^\circ$ for the *Central Caldera* and *Eastern Caldera* hydrophones.

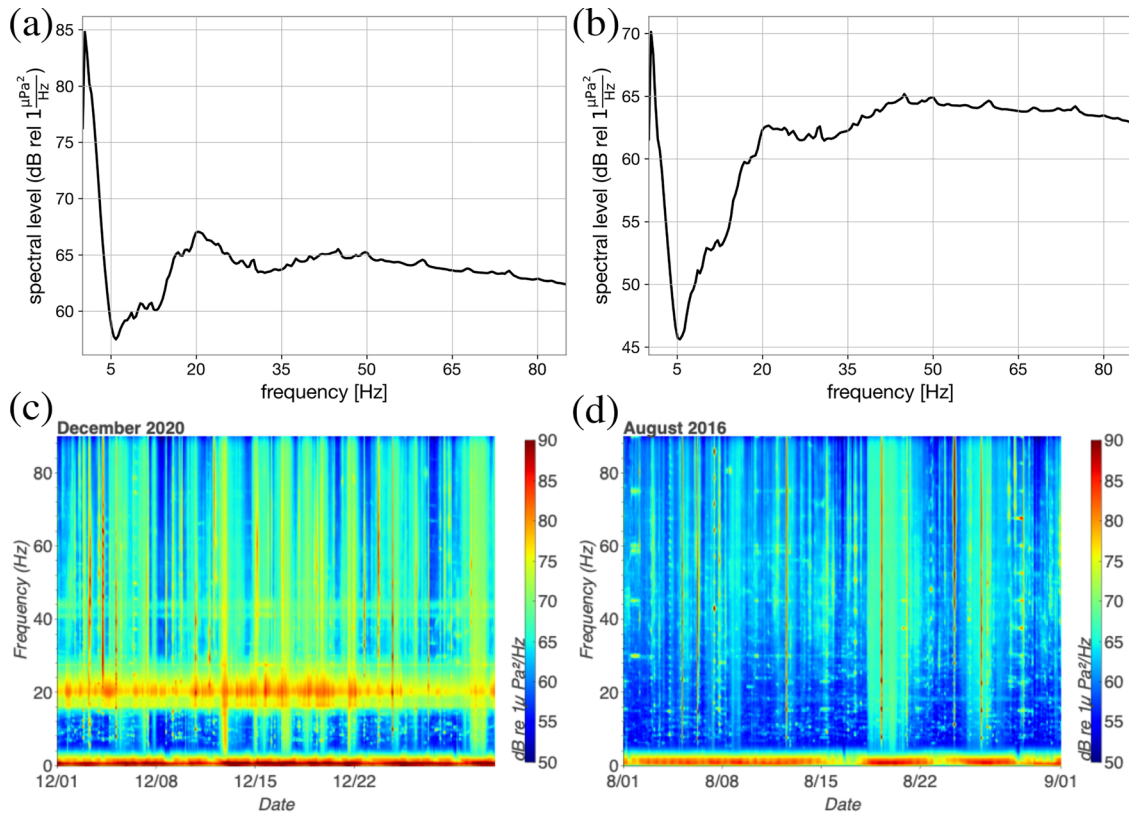


FIG. 3. (Color online) (a) Six-year PSD for the *Central Caldera* hydrophone. (b) Six-year PSD for the *Eastern Caldera* hydrophone. (c) Spectrogram containing fin whale vocalizations and shipping noise. Data is from *Central Caldera* and is from December 2020. (d) Spectrogram containing local shipping noise. Data is from *Central Caldera* and is from August 2016.

C. Acoustic simulation

Acoustic propagation between the *Eastern Caldera* hydrophone and the *Central Caldera* hydrophone was simulated using Kraken (Porter, 1992). CTD data from the *Axial Base* location (~ 20 km from the caldera hydrophones) was used to create a six year average sound speed profile [see

Fig. 1(b)]. Studying the seasonal fluctuations of arrival times is left for future work.

Due to the short range between the two hydrophones, peak spreading due to modal dispersion is negligible for the simulated TDGF. Therefore, a single arrival time is estimated to quantify the different arrivals. The arrival time is found by taking the argmax of each successive peak and

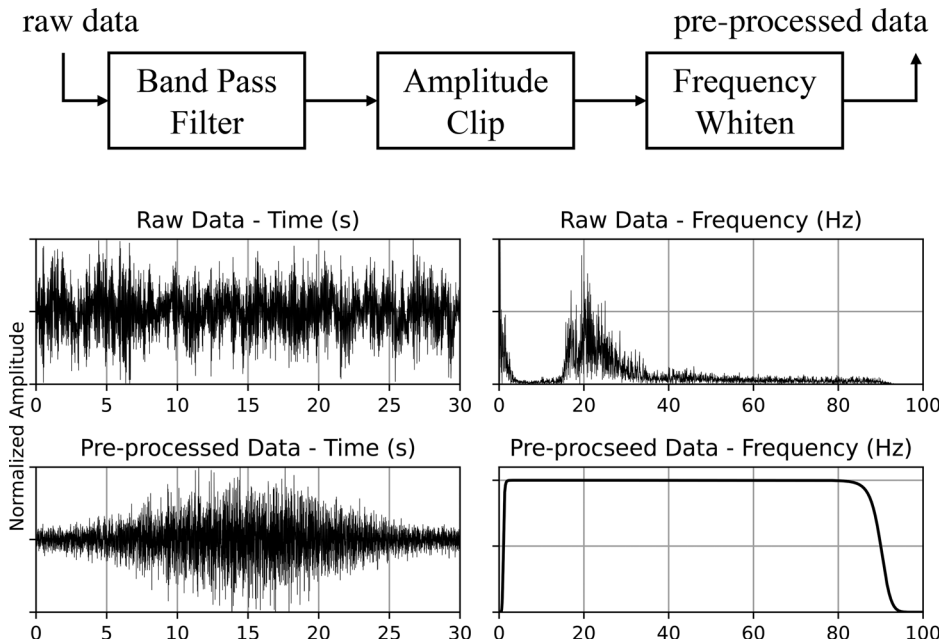


FIG. 4. Block diagram of the pre-processing methods. A 30 s section of data is shown before and after pre-processing in the time and magnitude frequency domain.

TABLE I. Simulated arrival times between *Central Caldera* and *Eastern Caldera* and the number of surface and bottom reflection for each propagation path.

Path label	Surface reflections	Bottom reflections	Simulated arrival time (s)
<i>d</i>	0	0	2.142
<i>s1b0</i>	1	0	2.959
<i>s2b1</i>	2	1	4.620
<i>s3b2</i>	3	2	6.473

using quadratic peak interpolation to get sub-time-bin resolution (Smith, 2011). Table I shows the simulated arrival times for the first four propagation paths. To succinctly reference different TDGF peaks, the following naming convention will be adopted throughout this paper. Each peak will have a name code of sXbY, where X corresponds to the number of surface reflections and Y corresponds to the number of bottom reflections. For NCCF peaks, A or B will be added to the end to designate a lag or lead peak respectively. For the direct path peak observed in the NCCF (see Sec. III A) the code dA will be used.

III. RESULTS

In Secs. III A, III B, and III C, the TDGF emergence, TDGF signal-to-noise ratio (SNR), and the long-term NCCF stack is presented.

A. Time domain Green's function emergence

Figure 5 shows a six-year average NCCF and the simulated arrival times given in Table I. The peaks that we see in the NCCF match the simulated arrival times. The negative time, or lag section, of the NCCF corresponds to acoustic propagation from *Central Caldera* to *Eastern Caldera*, and the TDGF peaks emerge from sound sources located in the endfire axis that is pointed towards Alaska (Fig. 2). The positive delay, or lead, section of the NCCF corresponds to acoustic propagation from *Eastern Caldera* to *Central*

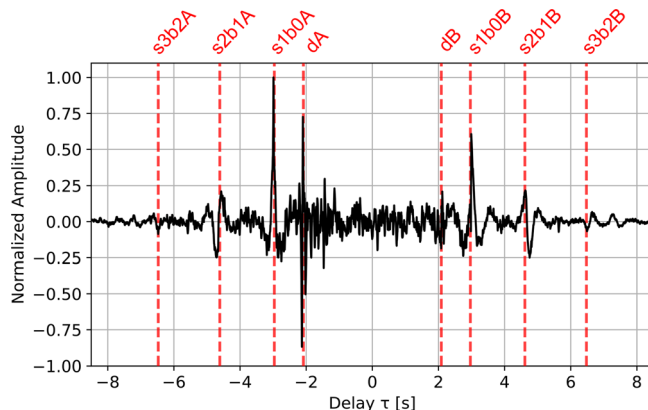


FIG. 5. (Color online) Six year average NCCF. Dashed lines indicate simulated arrival times given in Table I. From left to right, the simulated arrival times shown correspond to s3b2A, s2b1A, s1b0A, dA, dB, s1b0B, s2b1B, and s3b2B.

Caldera, and the TDGF peaks emerge from sound sources located in the endfire axis that is pointed towards the western coast of the United States (see Fig. 2). The peaks at ± 2.9 s correspond to an acoustic propagation path that reflects off of the surface of the ocean. The peaks at ± 4.62 s correspond to peaks that reflect off of the ocean surface twice and off of the ocean bottom once. The peak at -2.1 s corresponds to the direct path. The presence of the lag direct path peak and the absence of a lead direct path peak is likely due to the distribution of distant coherent sound sources.

In order to study the TDGF emergence, NCCFs were averaged for every month of the six years of data availability, resulting in 72 different emergence realizations. Figure 6 shows the TDGF emergence for all five distinguishable propagation paths. SNR is defined in Eq. (2) (Woolfe and Sabra, 2015), where $C_{peak}(\tau)$ is the user defined window containing a specific peak, and $C_{noise}(\tau)$ is defined as a window of the NCCF that contains only noise. Specifically, for the NCCF between *Central Caldera* and *Eastern Caldera*, $C_{noise}(\tau)$ is defined as the NCCF between -15 and -10 s, and the noise window is multiplied by the inverse of the auto-correlated Hann window to undo the windowing from pre-processing (Sec. II B),

$$SNR = 20 \cdot \log \left(\frac{\max(C_{peak}(\tau))}{3 \cdot \text{std}(C_{noise}(\tau))} \right). \quad (2)$$

A logarithmic curve [Eq. (3)] was fit to the mean emergence for all five peaks and is shown in Fig. 6. T_{avg} is the averaging time in hours and T_0 and A are constants. Theoretical studies show that the emergence of the impulse response should follow Eq. (3) for $A = 10$ under idealized conditions (Weaver and Lobkis, 2005), because coherent energy grows like T_{avg}^2 and incoherent energy grows like T_{avg} . In Fig. 6, the least squares fit is given for both Eq. (3) and for Eq. (3) with A fixed at 10. Brown *et al.* (2014) observe that with their data and hydrophone geometries, the emergence roughly follows Eq. (3) for $T_0 = 12$ hours and $A = 10$. For our data, hydrophone geometry, and sound distribution, we observe T_0 values for *dA*, *s1b0A*, and *s1b0B* for $A = 10$ around 3.5 or 4.5 h. For the *s2b1* peaks and $A = 10$, we observe T_0 values of around 30 h. However, the assumption of $A = 10$ does not seem to be particularly valid for the *s2b1* peaks with A values in the least-square fit being close to 7. This indicates that the ratio of coherent to incoherent noise actually grows like $T_{avg}^{0.7}$ instead of T_{avg} for the *s2b1* peaks,

$$SNR = A \cdot \log_{10} \left(\frac{T_{avg}}{T_0} \right). \quad (3)$$

B. Long-term signal-to-noise ratio

Figure 7 shows the long-term SNR and the 150-d smoothed, long-term SNR for each of the 5 distinguishable peaks with 201 h of averaging. There is a large seasonal pattern in the long-term SNR for the *dA* peak where larger SNR is seen in the summer months. This is caused by the seasonal 20 Hz feature described in Sec. III D. This is also the cause

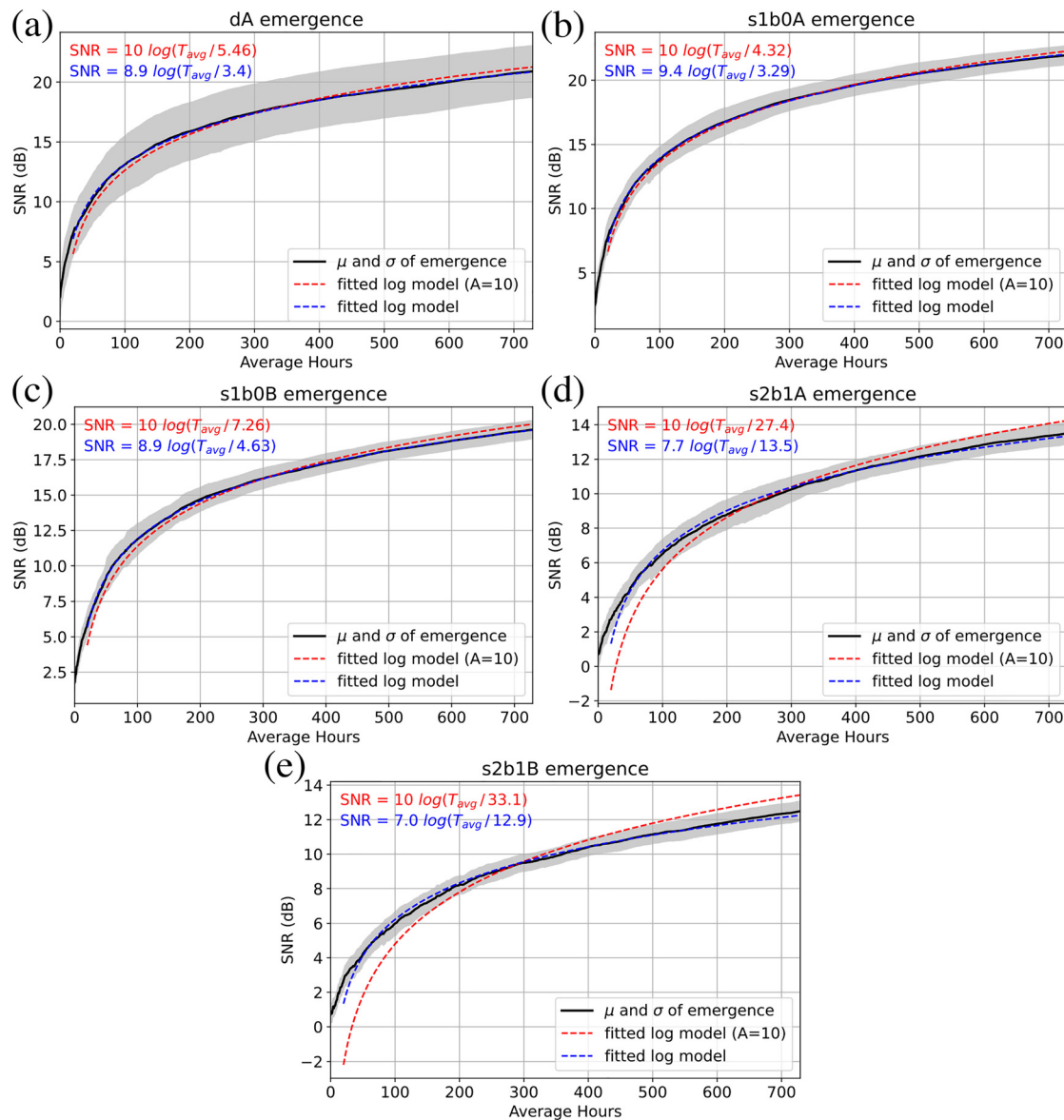


FIG. 6. (Color online) (a)–(e) TDGF emergence in the NCCF for specific acoustic propagation paths. The mean emergence is shown with the solid black line. The standard deviation of the emergence is shown with the shaded gray area. The red dashed line shows the least squares fit curve for Eq. (3) and $A = 10$. The blue dashed line shows the least squares fit curve for Eq. (3). The least-squared fit equations are given in the top left of each plot.

of the larger standard deviation of the emergence shown in Fig. 6(a). The *s1b0* peaks show a small annual fluctuation in the long-term SNR (Fig. 7). This could be due to the changing ocean environment or seasonal fluctuation in coherent sound sources distributions.

C. Long-term NCCF stack

Figure 8(a) shows the long term NCCF stack between the *Central Caldera* and *Eastern Caldera* hydrophones. Each NCCF consists of 201 h of average data comprised of the 100 h before and after the recorded time. The average time was selected using Fig. 6. However, due to non-constant data availability, each NCCF sample does not necessarily contain exactly 201 h of averaged ocean data. Figure 8(b) shows the actual number of average hours used

for each sample. Using the TDGF emergence information in Fig. 6, a threshold of 100 average hours (shown by the dashed line) is set and any sample below this threshold is considered invalid. The color bars in Fig. 8 indicate events occurring in the ocean including the axial seamount volcano eruption, fin whale vocalizations visible in the spectrograms of hydrophone data and an airgun experiment that happened directly over the hydrophones.

D. Fin whale chorus

There is an annual feature in the long-term NCCF stack (Fig. 8) that is centered on the dA peak around -2 s. The feature is about 1 s long in delay time and is present for roughly five months every year. Figure 9 shows a slice of a single NCCF while the feature is present. The frequency content

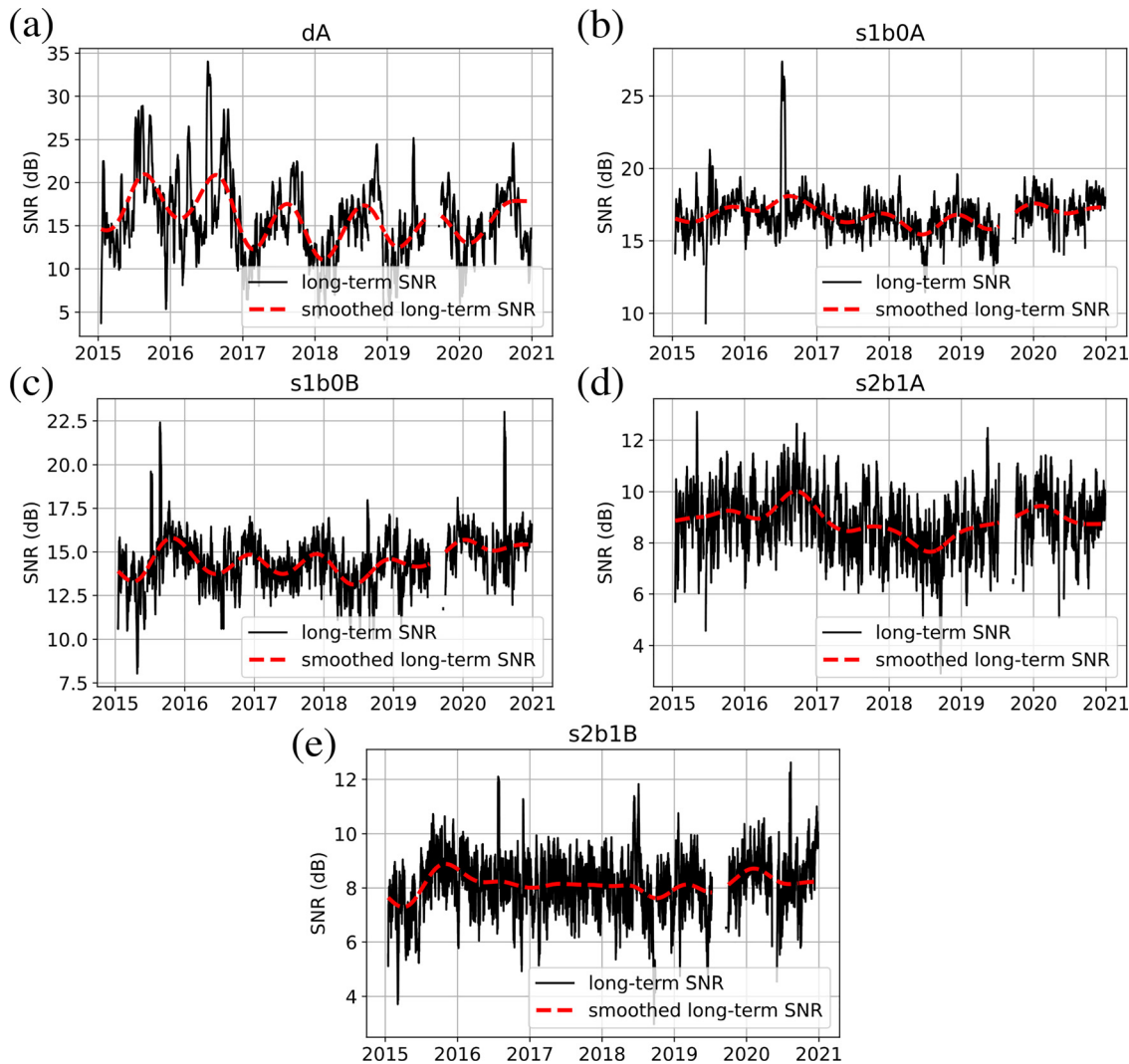


FIG. 7. (Color online) (a)–(e) Long-term SNR for every resolvable propagation path (solid line) and 150 day smoothed long-term SNR (dashed line) for 201 h of averaging.

of this feature is narrow band and is centered at 20 Hz. Figure 10 shows the spectrogram of the NCCF when the 20 Hz feature is and is not present. The energy at 7 Hz is present year-round, but the 20 Hz energy is seasonal. Due to the seasonal nature of this feature and the fact that it is 20 Hz, it is most likely caused by fin whales.

Interestingly, the annual pattern of the 20 Hz feature in the NCCF and the presence of 20 Hz fin whale calls in the spectrograms of ambient sound do not perfectly line up. Figure 11 compares the spectrum time-series of the two hydrophones to the spectrum time-series of the NCCF stack in the 20 Hz, one-third octave band. The spectrum time-series of the two hydrophones is created by taking the 601 h median of 15 min, 512 point PSD estimates, and then averaging over the 20 Hz, one-third octave band. The NCCF time series is created by taking the discrete Fourier transform of the entire 601 h average NCCF and then averaging over the 20 Hz, one-third octave band.

Our hypothesis to explain this difference in timing is that the fin whale calls that are visible in the spectrogram

and the 20 Hz signal in the NCCF are caused by different acoustic phenomena that both originate from fin whales. Sound that contributes to the *dA* peak is propagating horizontally in the water column and is located in the end-fire direction of the two hydrophones that is pointed towards Alaska (Fig. 2). Due to the horizontal propagation of the sound, it is likely from distant sources. Menze *et al.* (2019) document the presence of a fin whale chorus, in which the calls of many fin whales combine to a constant 20 Hz hum. In the fin whale chorus, there are no discernible discrete fin whale calls. This distant chorus is believed to contribute to the 20 Hz energy in the NCCF stack and is not clearly discernible in the spectrograms of ambient sound because it is buried in louder, local noise. When fin whale calls are visible in the spectrogram of ambient sound, individual calls are present in the signal and the calls likely originate from local fin whales. The pre-processing techniques outlined in Sec. II B are specifically designed to attenuate components of the received signal that have a large amplitude relative to the rest of the signal and components that have a strong,

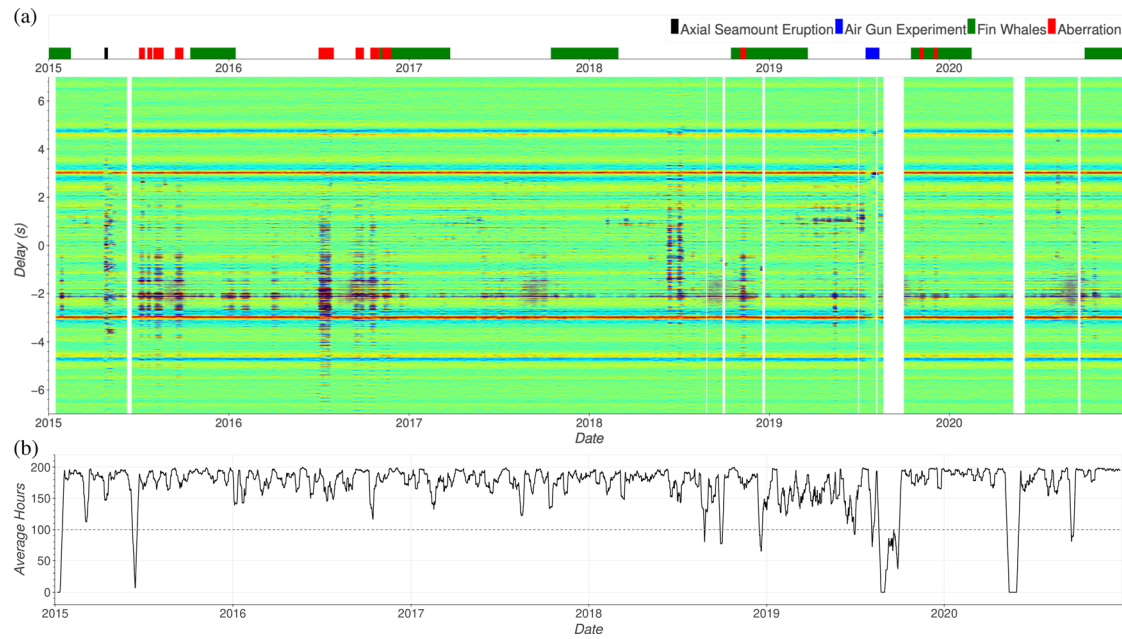


FIG. 8. (Color online) (a) Six year NCCF stack with average time of 201 h and stride of 1 h. Single NCCFs are considered invalid and shown as white if there are less than 100 h available for any given time during the six years. Important occurrences in the ocean are annotated above in color. (b) Plot of the number of available hours for any given NCCF sample and the valid NCCF threshold.

narrow frequency band. Both of these characteristics are representative of the fin whale calls that are visible in the spectrograms of ambient sound. This is why the contributions of local fin whale vocalizations are not visible in the NCCFs. The 20 Hz energy in the long-term NCCF stack and in the spectrograms of ambient sound are both likely due to fin whales. However, the 20 Hz energy in the NCCF stack is likely due a distant fin whale chorus with a rough directionality pointed towards Alaska. The 20 Hz energy in the ambient sound are likely due to local fin whale calls, where individual calls from single whales are visible. Very little is known about fin whale migration patterns, but they have been documented migrating from higher latitudes in the summer to lower latitudes in the winter (Mizroch *et al.*, 2009). This movement would be consistent with the patterns we see in the NCCF, where the energy in the *dA* peak is present in the summer/fall months.

IV. NCCF FEATURES

Throughout the six years of the long-term NCCF stack, there are several notable occurrences in the NCCF stack that

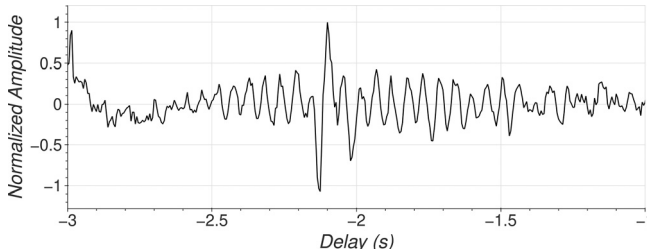


FIG. 9. Section of single NCCF when 20 Hz feature is present at the *dA* peak (-2.1 s). This NCCF is from 09-01-2017 00:00:00.

impact the quality of the TDGF estimate. Descriptions and explanations of some of these features are presented below.

Axial seamount volcanic eruption. In April 2015, the Axial Seamount volcano that the hydrophones are located in erupted (Wilcock *et al.*, 2016). This eruption is clearly visible in the NCCF stack and is shown in Fig. 12. During the eruption, discrete peaks are visible in the NCCF that are between the two direct path delay times of $\pm 2.1\text{ s}$. This is likely due to the directionality of coherent arrivals of

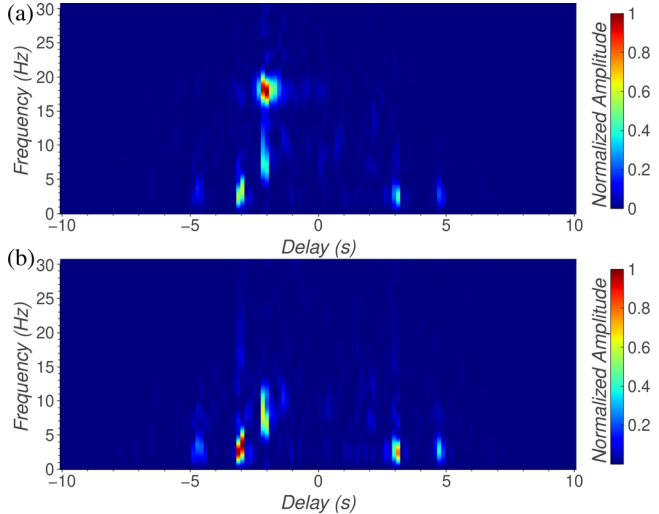


FIG. 10. (Color online) Spectrograms of NCCF when 20 Hz feature is present and not present. The spectrograms were calculated with a power spectral density estimate and the squared amplitude was normalized between zero and one. (a) Spectrogram of the NCCF when 20 Hz feature is present at the *dA* peak (-2.1 s). This NCCF is from 09-01-2017 00:00:00. (b) Spectrogram of NCCF when 20 Hz feature is not present. This NCCF is from 01-01-2018 00:00:00.

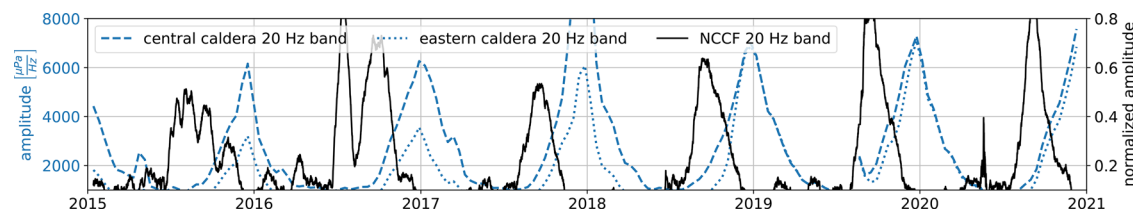


FIG. 11. (Color online) Timeline of fin whale vocalizations visible in the acoustic data and the 20 Hz feature visible in the long-term NCCF. There is a notable lag between energy in the NCCF and energy in the ambient sound that the NCCF is computed from. The 20 Hz energy in the NCCF is likely due to a distant fin whale chorus with directionality pointed toward Alaska, while the 20 Hz energy in the ambient sound is likely from local fin whale vocalizations.

impulsive sound sources that were emitted from the fissures (Wilcock *et al.*, 2016).

Air-gun experiment. In July and August of 2019, there was a seismic reflection survey that happened directly over the *Central Caldera* and *Eastern Caldera* hydrophones.⁴ Figure 13 shows the NCCF during this experiment. The noise in the NCCF decreases significantly during the air gun experiment. The actual incoherent noise levels in the ocean that are contributing to the noise levels in the NCCF are not expected to change during the duration of the air-gun experiment. The change in noise levels measured by the NCCF is due to the normalization that occurs in the frequency whitening step during pre-processing. The amplitude of the dA peak decreases during the course of the air gun experiment because the coherent sources that contribute to the dA peak are a distant source and are being drowned out by the local air gun sound sources. Different TDGF peaks fluctuate in amplitude over the course of the experiment. This is likely due to the changing location of the research vessel as it surveys the ocean floor. In future work, this data of opportunity could be used to experimentally explore the effect of local surface sound sources on multi-path arrivals.

Sporadic 7 Hz aberration. Another common aberration in the long-term NCCF stack is present sporadically throughout the six years of data but is more present in 2015 and 2016. Occurrences of this aberration are annotated as *Aberration* in Fig. 8(a). This feature is also centered around the dA peak and varies in relative amplitude and delay time length. The 1-h average, long-term NCCF stack reveals that the NCCF aberration turns on and off with an approximate period of 7 h [Fig. 14(a)]. The fast Fourier transform (FFT) of the 1-h NCCF stack [Fig. 14(b)] reveals that the frequency content of this aberration has a peak around 7 Hz and tapers off above around 20 Hz. Figure 14(c) shows the

spectrogram of the acoustic data from *Eastern Caldera* during this aberration. The 7 Hz sporadic aberrations are centered around the dA peak. This corresponds to a directionality of the sound sources causing these phenomena to be in the endfire axis that is pointed towards Alaska (see Fig. 2). The cause of this aberration in the NCCF stack is still unknown. Some possible explanations include distant acoustic surveying experiments, other unknown anthropogenic contributions, or seismic activity.

V. CONCLUSION AND DISCUSSION

In conclusion, noise interferometry was successfully used to estimate arrival times between two bottom-mounted hydrophones in the OOI Cabled Array separated by 3.2 km at an ocean depth of 1500 m. With an averaging time of 100 h or larger, direct, surface, and surface bottom reflected acoustic propagation paths are distinguishable throughout the six years of data. Further investigation shows that the direct path peak SNR fluctuates seasonally due to distant fin whale vocalizations. The single surface reflection propagation paths display a small seasonal variation. For dA, s1b0, and s2b1 peaks, the SNR is stable throughout the six years of data that is analyzed. A long-term noise cross correlation (NCCF) stack was constructed for six years of available data to assess the quality of the NCCF. Effects on the NCCF stack were observed from the Axial seamount volcano, a local seismic reflection survey, and seasonal fin whale vocalizations. A fin whale chorus is shown to be detectable with the NCCF that is separate from the local fin whale vocalizations that are present in power spectral time-series of individual hydrophones.

Given the size of the dataset and the quality of multi-path arrivals in the NCCF throughout the six years of data,

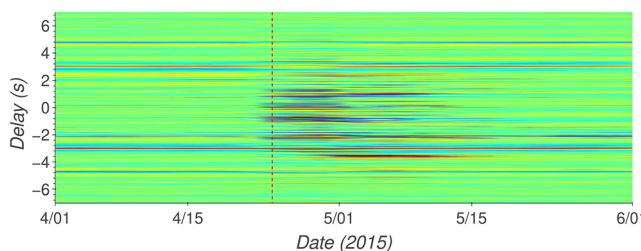


FIG. 12. (Color online) NCCF stack during Axial Seamount eruption in April 2015. Dashed line indicates the beginning of the eruption. Effects in the NCCF before dashed line are due to average time window.

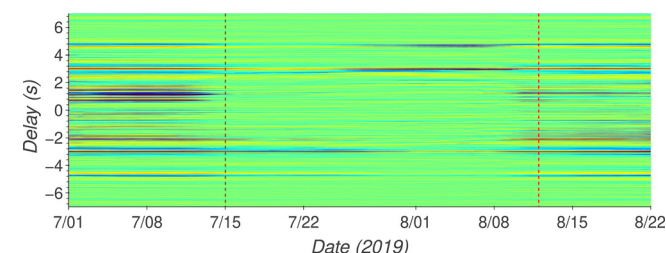


FIG. 13. (Color online) NCCF stack during the seismic reflection experiment during July and August 2019. Dashed lines indicate the beginning and end of the experiment. Effects in the NCCF before or after the dashed line are due to the average time window.

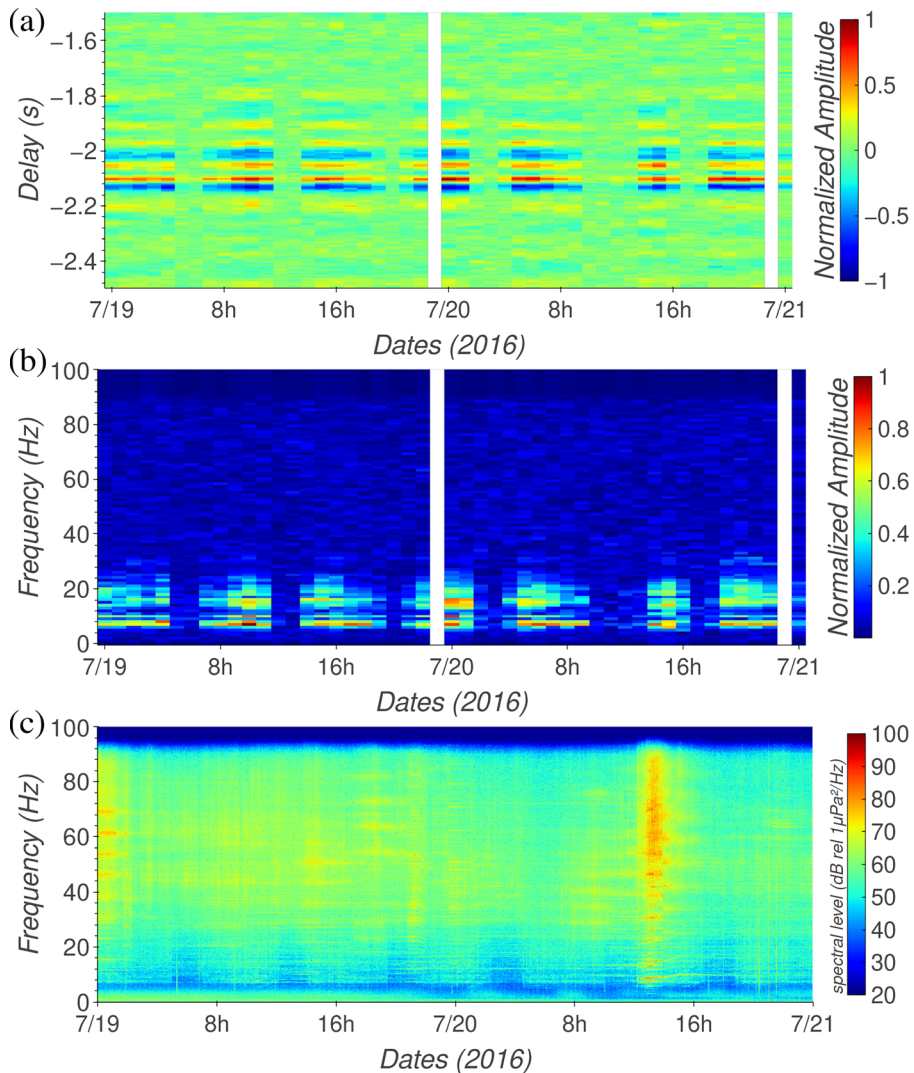


FIG. 14. (Color online) (a) 1-h average NCCF during occurrences of 7 Hz NCCF aberration. Data is from July 19–21, 2016. (b) Magnitude of the FFT of the NCCF window shown in (a). (c) Spectrogram of hydrophone data from the *Eastern Caldera* hydrophone during the 7 Hz aberration.

there are many opportunities for future explorations using this data. Some potential future directions are discussed below.

There is some relevant information contained in the NCCF stack that is unrelated to the TDGF estimate. For some loud features in the ocean, such as the Axial Seamount volcanic eruption, directional information could be inferred from the NCCF stack. The effects of fin whale vocalizations on the NCCF stack could also potentially be developed into new ways to monitor fin whale population and migration. We were able to measure energy from the fin whale chorus that was not clearly visible in individual spectrograms of raw data. Similarly, while there is still no clear explanation for the 7 Hz sporadic aberration described in Sec. III, it is interesting that this coherent sound source is able to be clearly detected even though it is not as clearly visible in the PSD of either hydrophone. In future developments, these features of the NCCF could be leveraged to learn information about the ocean.

The results in this paper lay the necessary ground work for developing long-term ocean monitoring techniques using multi-path arrivals estimated with ambient noise

interferometry. Since multi-path arrivals traverse the entire water column, they can be used to infer information about the entire water column. This is an advantage over direct path propagation which can only characterize ocean properties along the eigenray connecting the two nodes. Demonstrating the ability to reliably distinguish the TDGF with hydrophones in an ocean observatory with bottom-mounted hydrophones in the deep ocean also points towards to possibility of scaling up these techniques for global ocean monitoring. According to Munk *et al.* (1995, p. 197), the root-mean-squared-error of an arrival time estimate is a function of the SNR. In future works, models can potentially be developed to invert arrival time estimates to estimate oceanographic variables such as water column sound speed. The analysis presented in this paper can be used to assess the error bounds of these model predictions.

The seismic reflection survey conducted in 2019 directly over the two hydrophones provides a unique opportunity for further investigation into the technique of noise interferometry. Several papers have developed simulation techniques to analytically observe the effects of different sound distributions (Larose *et al.*, 2006; Sabra *et al.*, 2005b;

Skarsoulis and Cornuelle, 2019). Since the airgun is an impulsive sound source, this data of opportunity could lead to experimental evidence on how local sound sources contribute to the multi-path arrivals.

The quality of the long-term NCCF stack and the reliability of distinguishing multi-path arrivals throughout the six years of data shows promise for future developments in ocean monitoring applications, and is a promising direction of future investigations.

ACKNOWLEDGMENTS

This research was supported by the Office of Naval Research Grant No. N00014-19-1-2644. The authors would also like to thank Dr. William Wilcock for valuable discussion about the microseism band and Dr. Kathleen Stafford for valuable discussions about the fin whale chorus.

¹NFS Ocean Observatories Initiative Data Portal, <https://ooinet.oceanobservatories.org> Low-Frequency Acoustic Receiver(network:OO, station:AXCC1). Downloaded on 29 January 2021.

²NFS Ocean Observatories Initiative Data Portal, <https://ooinet.oceanobservatories.org> Low-Frequency Acoustic Receiver(network:OO, station:AXEC2). Downloaded on 29 January 2021.

³For more information, see <http://ds.iris.edu/gmap/>.

⁴For more information, see Cruise DOI:10.7284/908292.

Bensen, G. D., Ritzwoller, M. H., Barmin, M. P., Levshin, A. L., Lin, F., Moschetti, M. P., Shapiro, N. M., and Yang, Y. (2007). “Processing seismic ambient noise data to obtain reliable broad-band surface wave dispersion measurements,” *Geophys. J. Int.* **169**(3), 1239–1260.

Boué, P., Denolle, M., Hirata, N., Nakagawa, S., and Beroza, G. C. (2016). “Beyond basin resonance: Characterizing wave propagation using a dense array and the ambient seismic field,” *Geophys. J. Int.* **206**(2), 1261–1272.

Brooks, L. A., and Gerstoft, P. (2009). “Green’s function approximation from cross-correlations of 20–100hz noise during a tropical storm,” *J. Acoust. Soc. Am.* **125**(2), 723–734.

Brown, M. G., Godin, O. A., Williams, N. J., Zabotin, N. A., Zabotina, L., and Bunker, G. J. (2014). “Acoustic green’s function extraction from ambient noise in a coastal ocean environment,” *Geophys. Res. Lett.* **41**(15), 5555–5562, <https://doi.org/10.1002/2014GL060926>.

Brown, M. G., Godin, O. A., Zang, X., Ball, J. S., Zabotin, N. A., Zabotina, L. Y., and Williams, N. J. (2016). “Ocean acoustic remote sensing using ambient noise: Results from the florida straits,” *Geophys. J. Int.* **206**(1), 574–589.

Denolle, M. A., Dunham, E. M., Prieto, G. A., and Beroza, G. C. (2013). “Ground motion prediction of realistic earthquake sources using the ambient seismic field,” *J. Geophys. Res. Solid Earth* **118**(5), 2102–2118, <https://doi.org/10.1029/2012JB009603>.

Evers, L., Wapenaar, K., Heaney, K., and Snellen, M. (2017). “Deep ocean sound speed characteristics passively derived from the ambient acoustic noise field,” *Geophys. J. Int.* **210**(1), 27–33.

Godin, O. A. (2009). “Accuracy of the deterministic travel time retrieval from cross-correlations of non-diffuse ambient noise,” *J. Acoust. Soc. Am.* **126**(6), EL183–EL189.

Godin, O. A. (2010). “Cross-correlation function of acoustic fields generated by random high-frequency sources,” *J. Acoust. Soc. Am.* **128**(2), 600–610.

Godin, O. A. (2018). “Acoustic noise interferometry in a time-dependent coastal ocean,” *J. Acoust. Soc. Am.* **143**(2), 595–604.

Godin, O. A., Katsnelson, B. G., Qin, J., Brown, M. G., Zabotin, N. A., and Zang, X. (2017). “Application of time reversal to passive acoustic remote sensing of the ocean,” *Acoust. Phys.* **63**(3), 309–320.

Goncharov, V. V., Vedenev, A. I., Shatrevan, A. V., Shurup, A. S., Sergeev, S. N., Godin, O. A., Zabotin, N. A., and Brown, M. G. (2015). “Tomographic inversion of measured cross-correlations of ambient noise in shallow water using the ray theory,” *Proc. Mtgs. Acoust.* **24**(1), 070005.

Groos, J. C., Bussat, S., and Ritter, J. R. R. (2012). “Performance of different processing schemes in seismic noise cross-correlations,” *Geophys. J. Int.* **188**(2), 498–512.

Larose, E., Margerin, L., Arnaud, D., Tiggelen, B., Campillo, M., Shapiro, N., Paul, A., Stehly, L., and Tanter, M. (2006). “Correlation of random wavefields: An interdisciplinary review,” *Geophys. Soc. Explorat. Geophysicists* **71**, SI11–SI21.

Menze, S., Zitterbart, D., Biuw, M., and Boebel, O. (2019). “Estimating the spatial distribution of vocalizing animals from ambient sound spectra using widely spaced recorder arrays and inverse modelling,” *J. Acoust. Soc. Am.* **146**(6), 4699–4717.

Mizroch, S. A., Rice, D. W., Zwiefelhofer, D., Waite, J., and Perryman, W. L. (2009). “Distribution and movements of fin whales in the north pacific ocean,” *Mammal Rev.* **39**(3), 193–227.

Munk, W., Worcester, P., and Wunsch, C. (1995). *Ocean Acoustic Tomography* (Cambridge University Press, Cambridge, UK).

Porter, M. B. (1992). “The KRAKEN normal mode program,” <https://apps.dtic.mil/sti/citations/ADA252409> (Last viewed 8/18/2021).

Roux, P., and Kuperman, W. A. (2004). “Extracting coherent wave fronts from acoustic ambient noise in the ocean,” *J. Acoust. Soc. Am.* **116**(4), 1995–2003.

Roux, P., Sabra, K. G., Kuperman, W. A., and Roux, A. (2005). “Ambient noise cross correlation in free space: Theoretical approach,” *J. Acoust. Soc. Am.* **117**(1), 79–84.

Sabra, K. G., Gerstoft, P., Roux, P., Kuperman, W. A., and Fehler, M. C. (2005a). “Surface wave tomography from microseisms in southern california,” *Geophys. Res. Lett.* **32**(14), L14311, <https://doi.org/10.1029/2005GL023155>.

Sabra, K. G., Roux, P., and Kuperman, W. A. (2005b). “Arrival-time structure of the time-averaged ambient noise cross-correlation function in an oceanic waveguide,” *J. Acoust. Soc. Am.* **117**(1), 164–174.

Sambell, K. A. M., Smets, P. S. M., Simons, D. G., Snellen, M., and Evers, L. G. (2019). “A study on the ambient noise field at a hydroacoustic array near robinson crusoe island,” *Geophys. J. Int.* **218**(1), 88–99.

Schwock, F., and Abadi, S. (2021). “Statistical properties of a modified welch method that uses sample percentiles,” in *Proceedings of the 2021 IEEE International Conference on Acoustics, Speech and Signal Processing (ICASSP)*, June 6–11, Toronto, Canada, pp. 5165–5169.

Schwock, F., Ragland, J., Setiawan, L., Munson, M., and Abadi, S. (2021). “ooipy/ooipy: OOIPy v1.1.2: A Python toolbox designed to aid in the scientific analysis of Ocean Observatories Initiative (OOI) data,” <https://doi.org/10.5281/zenodo.4747784>.

Skarsoulis, E. K., and Cornuelle, B. D. (2019). “Cross-correlation of shipping noise: Refraction and receiver-motion effects,” *J. Acoust. Soc. Am.* **145**(5), 3003–3010.

Smith, J. O. (2011). *Spectral Audio Signal Processing* (W3k Publishing).

Urick, R. J. (1975). *Principles of Underwater Sound*, 2nd ed. (McGraw-Hill, New York), p. 185.

Watkins, W. A., Tyack, P., Moore, K. E., and Bird, J. E. (1987). “The 20-Hz signals of finback whales (*balaenoptera physalus*),” *J. Acoust. Soc. Am.* **82**(6), 1901–1912.

Weaver, R. L., and Lobkis, O. I. (2001). “Ultrasonics without a source: Thermal fluctuation correlations at MHz frequencies,” *Phys. Rev. Lett.* **87**(13), 134301.

Weaver, R. L., and Lobkis, O. I. (2004). “Diffuse fields in open systems and the emergence of the green’s function (I),” *J. Acoust. Soc. Am.* **116**(5), 2731–2734.

Weaver, R. L., and Lobkis, O. I. (2005). “Fluctuations in diffuse field-field correlations and the emergence of the Green’s function in open systems,” *J. Acoust. Soc. Am.* **117**(6), 3432–3439.

Webb, S. C. (1992). “The equilibrium oceanic microseism spectrum,” *J. Acoust. Soc. Am.* **92**(4), 2141–2158.

Wenz, G. M. (1962). “Acoustic ambient noise in the ocean: Spectra and sources,” *J. Acoust. Soc. Am.* **34**(12), 1936–1956.

Wilcock, W. S. D., Tolstoy, M., Waldhauser, F., Garcia, C., Tan, Y. J., Bohnenstiel, D. R., Caplan-Auerbach, J., Dziak, R. P., Arnulf, A. F., and Mann, M. E. (2016). “Seismic constraints on caldera dynamics from the 2015 Axial Seamount eruption,” *Science* **354**(6318), 1395–1399.

Woolfe, K. F., Lani, S., Sabra, K. G., and Kuperman, W. A. (2015). “Monitoring deep-ocean temperatures using acoustic ambient noise,” *Geophys. Res. Lett.* **42**, 2878–2884, <https://doi.org/10.1002/2015GL063438>.

Woolfe, K., and Sabra, K. (2015). “Variability of the coherent arrivals extracted from low-frequency deep-ocean ambient noise correlations,” *J. Acoust. Soc. Am.* **138**, 521–532.